Compression Behavior of 3D Printed Polymer TPU Cubic Lattice Structure

Chenfan Zhang[a], Teng Li[a], Qingtian Deng[a]* , Xinbo Li[a]

[a]Chang'an University, School of Science, Xi'an, 710064, China.

Based on the face-centered cubic structure, several different types of cubic lattice structures are designed in this paper, the quasi-static compression behavior of the lattice structure is thoroughly investigated by finite element simulation and experimental testing, in which mechanical properties and energy absorption capacities are summarized. The experimental specimens made from thermoplastic polyurethane TPU are additively manufactured using the fused deposition technology. Effects of strut style, strut distance, arrangement form, curvature, and several honeycomb lattice structures are considered. The results show that: under the condition of the same relative density, the selection of sinusoidal struts with larger curvature, the arrangement of 45°/135°, and the inward gradient of the strut distance can all improve the energy absorption characteristics of the structure. Compared with the traditional face-centered cubic structure (specimen L-1), the SEA of the structure with the strut curvature of 0.25, the 45°/135° arrangement of the sinusoidal struts, and the inward gradient of the strut distance is improved by 64% , 190%, and 107%; the introduction of a honeycomb structure with a high relative density can effectively resist the buckling deformation of the structure, and the SEA of the triangular, re-entrant and hexagonal honeycomb structures are 354%, 603% and 548% higher than that of the basic structure, respectively. In addition, reducing the lattice height also resists destabilization.

Keywords: *Cubic lattice structure, Energy absorption, Strength, Honeycomb structure.*

1. Introduction

Lattice structure has light weight, strong energy absorption properties and high impact resistance[1,2], many scholars have carried out a lot of researches on this,the researches have covered abroad ranges in the design[3-6], fabrication[7,8] and optimization[9-11] of lattice structure. Nasim and Galvanetto[12] compared the specific mechanical properties of all eight lattice structures under the same geometric parameters, and obtained the loading conditions for the structure to have good stiffness, strength and energy absorption. Mahbod et al.[13] investigated the elastoplastic mechanical properties of regular and functionally graded superimposed porous structures composed of bipyramidal dodecahedral unit cells. The surrogate models of elastic and plastic mechanical properties are established through single-objective and multi-objective optimization. The results show that this optimization leads to a significant improvement in the performance of regular and functionally graded porous structures. Teimouri and Asgari[14] introduced solid unit cells and thin-walled shell unit cells based on a topology optimization (TO) method for generating ideal regular and functionally graded lattice structures. It is found that the porosity directly affects the mechanical properties and crushing parameters of the solid lattice structure, while for the shell-type structure, better mechanical properties can be obtained even with a smaller material usage ratio. Due to the designability of the lattice structure, the researchers carried out optimization based on the previous research results, using

theoretical and numerical optimization methods to design and propose a new lattice structure, which mechanical properties are significantly improved compared with the traditional structure. Based on the Bidirectional Evolutionary Structural Optimization (BESO) method, Teimouri et al.[15] combined grid wireframes based on different support structures into a topology-optimized solid structure. The results show that the mechanical properties of the new hybrid solid lattice structure in terms of stiffness, buckling failure load and energy absorption are improved compared with pure solid structure and lattice structure. Alomar and Concli[16] designs a new type of lattice structure made of Ti6Al4V with a circular-based constituent cell, then performance comparison with other types of lattices was accomplished via mechanical properties-relative density plots. The numerical results showed an evenly distributed stress within the microstructures of the circular cells. Additionally, the new cell exhibited higher load-bearing capacity and stiffness in comparison with the BCC cell of higher relative density. Ding et al.[17] proposed a new lattice structure ARCH, and experimentally studied that the ARCH lattice structure has better mechanical properties and energy absorption capabilities than the traditional lattice structure. In addition, some excellent properties of biomimetic structures are also used in the optimal design of lattice structures. Yang and Li[18] fabricates a cuttlebone-like lattice (CLL) material is obtained and its deformation behavior and compressive properties under impact loads are investigated. The results show that the CLL material undergoes a buckling-dominated and layer-by-layer deforming process, the CLL material outperforms a broad range of existing cellular materials in

terms of relative collapse strength, relative elastic modulus and SEA. Inspired by the arrangement of metal atoms and bones, Wei et al.[19] proposed a new multi-biomimetic strategy that combines a light-weight and high-specific-strength face-centered cubic structure with a high-toughness concentric structure. Compared to the 20% metamaterial, the strain and absorbed energy at the onset of fracture of the rod are 2 and 3.8 times, respectively, those of the pure hard phase lattice.

Due to the internal complexity of the lattice structure, it cannot be obtained by traditional fabrication techniques,in recent years, selective laser sintering (SLS) and selective laser melting (SLM) and other additive manufacturing technologies[20-22] have been applied in many fields as new process fabrication technologies, which greatly facilitate the fabrication of complex structures. Verma et al.[23] uses the design freedom provided by 3D printing to create a lattice structure on a metal substrate, which is used as a mechanical interlock between the polymer resin and the metal during the injection molding process, solve the interface connection problem of metal and reinforced plastic. Wang et al.[24] chose the laser melting technology and added 316L steel to make the lattice structure. The results show that this lattice has better energy absorption capacity than conventional FCC lattices. Additive manufacturing technology solves many problems that cannot be solved by traditional preparation methods by virtue of its novel forming technology and the precision of printed specimens. To overcome the difficult problem of removing support materials, Li et al.[25] using multiple inkjet printing plastic 3D printers combined with wax removal process to produce on a centimeter scale. The results show that by using additive manufacturing with different constituent materials, such as alloys and ceramics, semi-plate-based lattice materials can be manufactured to offer greater potential in engineering design than traditional truss-based lattice materials. To address issues of slanting and cluttering, Kostadinov et al.[26] studied the feasibility of using SLM for vertically oriented porous structures, the preliminary results indicate that structures such as shell reinforcements and bioinspired unit cells reduce the occurrence of slanting and cluttering and might serve as interim solutions for the printing of large filigree structures. In addition, Silva et al.[27] explored the capabilities of fuse filament fabrication (FFF) to produce miniature lattices, the results showed that it was possible to print functional 3D miniature open cell polymer lattice structures without support.

At present, materials with a lattice structure prepared by additive manufacturing technology are mostly found in titanium alloys, stainless steel and other metal materials, and the mechanical properties and failure modes of this lattice structure are basically the same. However, superelastic foam rubber has physical properties such as light weight, easy pore formation, and compressibility[28-30], and is mostly used in shock-absorbing[31] and impact-resistant materials[32]. It exhibits good load-bearing properties and damage resistance in uniaxial compression tests. Therefore, this paper selects a substrate with the above properties—tpu thermoplastic polyurethane elastomer rubber[33]—and combines it with a complex, controllable porous lattice structure. Thus, a soft and highly elastic lattice structure is prepared. In addition, the present research mainly focuses on the traditional lattice

structure, and there is little research on the mechanical properties of the hierarchical face-centered cubic lattice structure. Only Wanget al.[34] improved the traditional face-centered cubic lattice (FCC), and the results showed that the new structure have larger platform stress and better energy absorption performance than the traditional FCC lattice. In this paper, based on the traditional face-centered cubic lattice (FCC), Parametric studies are carried out to investigate the influence of various geometric parameters and designed the hierarchical lattice structure including geometric parameters such as strut distance, style, curvature, arrangement form, etc. In addition, introduced the lattice structure of triangular[35], re-entrant[36], and hexagonal honeycomb[37,38] configurations, the compression behavior of the structure was tested through uniaxial compression experiments, and the influence of geometric parameters and honeycomb configuration on the mechanical properties of the structure was evaluated.

2. Materials and Methods

2.1. Design approach

The traditional face-centered cubic structures are widely used in many fields due to its excellent mechanical properties. To explore the influence of geometric parameters on the mechanical properties of the structure, it is necessary to study the strut style, strut distance and arrangement of the structure. Based on the cubic lattice structure with orthogonal (0°/90°) arrangement between each layer as shown in Figure 1a, design approaches of the structure is carried out by changing the internal geometric parameters of the structure, in which the first approach is changing the strut distance, and taking the strut distance as 1mm, 2mm, and 3mm respectively. The second approach is changing the strut style and introducing a sine curve instead of a straight line, the amplitude of the sine curve is represented by H, and the unit length is L, the curvature of the sine curve is represented by k, k=H/L. The third approach is changing the line arrangement style, taking two forms: cross orthogonal (0°/90°) and diagonal orthogonal (45°/135°). The fourth approach is introducing the strut distance of the gradient form, taking the strut distance from 2mm to 4mm respectively, and taking two gradient forms: outward gradient and inward gradient. The fifth approach introduces a porous honeycomb structure, which are triangle, re-entrant, and regular hexagon respectively. The size specifications of all lattice structures as shown in Table 1.

2.2. Manufacturing of specimens

The specimen size is choosing to be 49mm×49mm×49mm, which is made by elastomer composite material thermoplastic polyurethane (TPU) using fused deposition method (FDM) technology, and TPU material parameters as shown in Table 2. At first, SOILDWORKS software is used to build a three-dimensional model, and the file is saved as .stl format, after importing the slicing software JGcreate, the printing parameters are set, including layer height 0.2mm, printing temperature 220°, platform temperature 50°, and printing speed 10mm/s. After slicing, the file is saved as .gcode format, importing the SD card and connect to 3D printer for fabrication. Figure 2 shows the printed specimens.
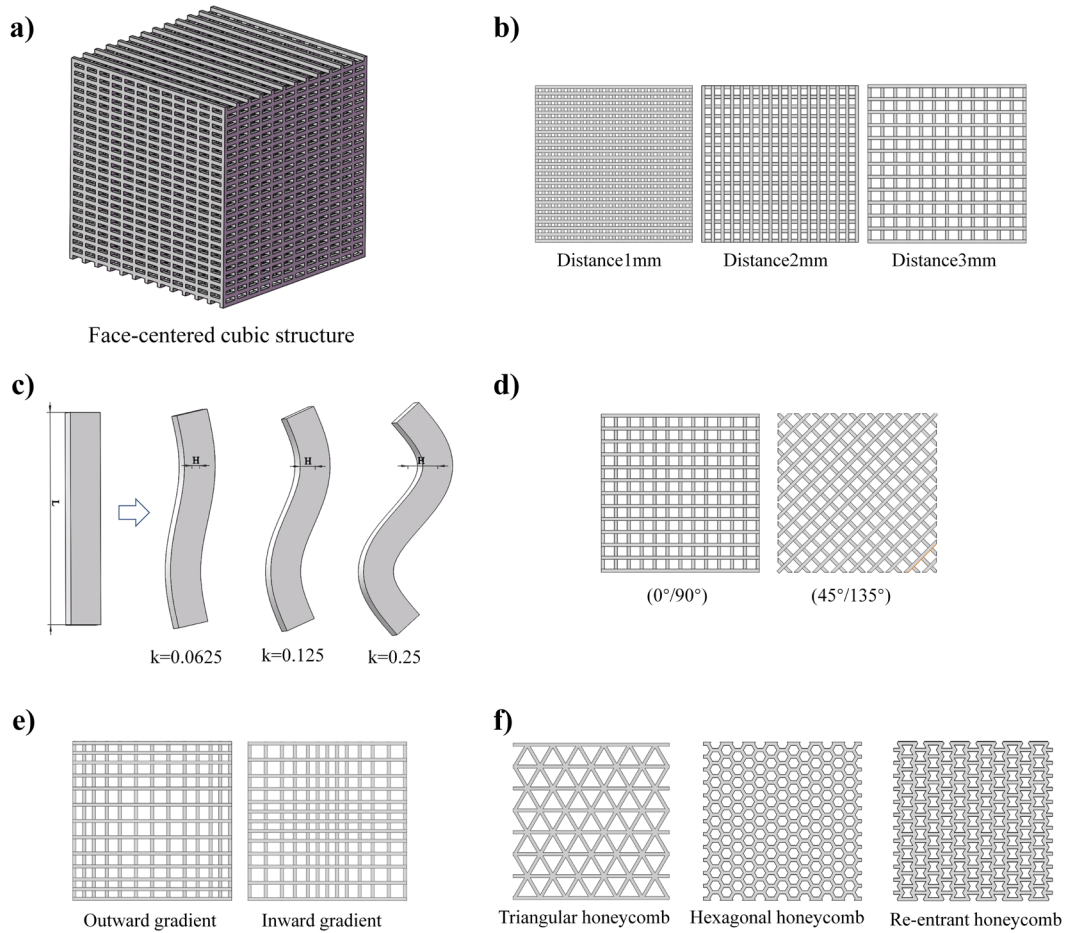
Figure 1. a) Traditional face-centered cubic structure, b) Different strut distance, c) Different curvature, d) Different arrangement forms, e) Strut distance in gradient form, f) Several porous honeycomb structures.

Table 1. Specification of lattice structure parameters.

structure	strut distance(mm)	mass(g)	Strut style	Micro-space structure
L-1	3	29.6	Straight line	(0°/90°) Orthogonal
L-2	2	48.05	Straight line	(0°/90°) Orthogonal
L-3	1	67.9	Straight line	(0°/90°) Orthogonal
L-4	2-4	37.53	Straight line	Inward gradient
L-5	4-2	37.72	Straight line	Outward gradient
L-6	3	39.33	Straight line	(45°/135°) Orthogonal
L-7	3	36.84	Sine curve(k=0.0625)	(0°/90°) Orthogonal
L-8	3	40.9	Sine curve(k=0.125)	(0°/90°) Orthogonal
L-9	3	49.04	Sine curve(k=0. 25)	(0°/90°) Orthogonal
L-10	2-4	40.24	Sine curve(k=0.0625)	Inward gradient
L-11	4-2	37.24	Sine curve(k=0.0625)	Outward gradient
L-12	3	40.11	Sine curve(k=0.0625)	(45°/135°) Orthogonal
L-13	3	36.95	Straight line/ Sine curve(k=0.0625)	(0°/90°) Orthogonal
L-14	/	61.08	Triangular honeycomb	(0°/90°) Orthogonal
L-15	/	73.20	Re-entrant honeycomb	(0°/90°) Orthogonal
L-16	/	67.25	Hexagonal honeycomb	(0°/90°) Orthogonal

Table 2. TPU material parameters.

Material	Density/g·cm⁻³	Elastic Modulus/MPa	Poisson's ratio	Tensile Strength/MPa
TPU	1.43	7.4	0.47	18.74

2.3. Manufacturing defects of 3D printing

To characterize the manufacturing defects of the specimens under the same density, according to literature[39], the relative density $\bar{\rho}$ of each specimen was calculated according to the Equation 1, as shown in Table 3. Combining with Table 1, it can be seen that under the condition of the same relative density, the quality of each specimen is different, and the measured quality of each specimen is lower than the ideal quality. The inter fiber bonding, interlayer bonding, and filling effect seriously affect the quality and performance. In the process of specimen preparation, there are problems such as uneven filling, weak adhesion, and residual silk in the gaps. These problems can cause printing defects in the specimens, which is why the simulation results do not match the experimental results.
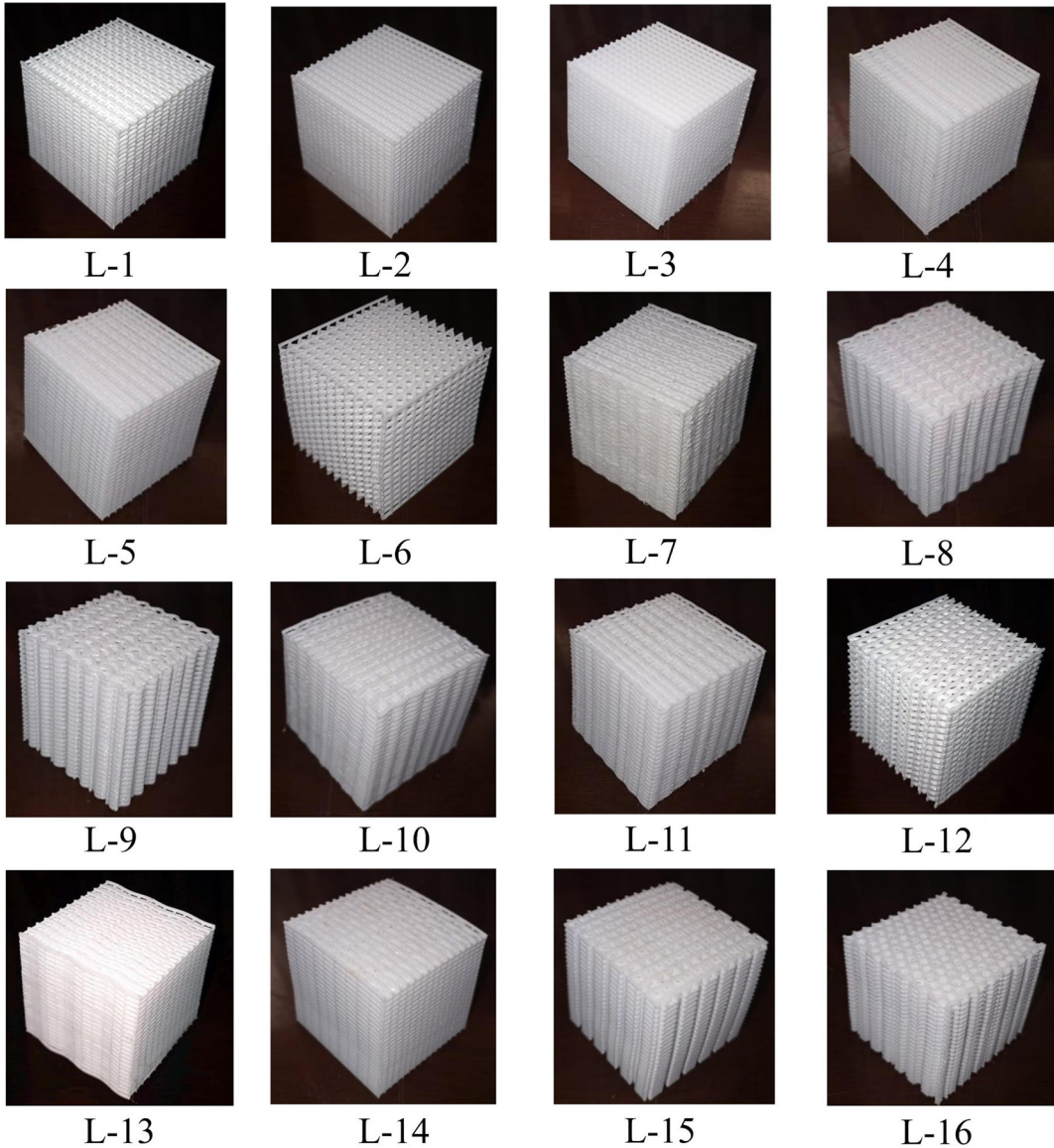
Figure 2. Cubic lattice specimen fabricated by 3D printing.

Table 3. Relative density of specimens.

Specimen	L-1	L-2	L-3	L-4	L-5	L-6	L-7	L-8
$\bar{\rho}$	0.265	0.347	0.51	0.265	0.265	0.25	0.272	0.265
Specimen	L-9	L-10	L-11	L-12	L-13	L-14	L-15	L-16
$\bar{\rho}$	0.313	0.281	0.265	0.312	0.269	0.42	0.528	0.439

$$\bar{\rho} = \frac{V_s}{V_c} \qquad (1)$$

where V_s is the specimen volume, V_c is the apparent volume. Except for the strut distance and the lattice structure of the two variables of the porous honeycomb, the relative densities of the other specimens are basically the same.

2.4. Experimental tests

The electronic universal testing machine CMT5305 (Figure 3a) was used to conduct a quasi-static uniaxial compression experiment. The loading method as shown in Figure 3b, the specimen was placed on a fixed supporting plate, loaded by the loading plate, in which the compressive strain is set to be 70% of the height of the specimen. To ensure the quasi-static loading conditions, the loading rate is maintained at 1mm/min, the displacement and compression force of the loading platform are recorded by sensors. During the whole compression experiment, a industrial camera was used to take a snapshot of the specimen for the analyze. In order to avoid chance, 2 specimens were prepared for each working condition and tested one by one, and finally the mean value of the two curves was taken for analysis.

Figure 4 selects two experimental test curves of several representative structures, same as the test results of the rest of the structures, it showed that the two test results are basically consistent, which well verifies the repeatability of the results. However, due to printing defects of different degrees in the preparation of specimens, the two curves also show some inconsistency, which is manifested in the stress plateau stage, namely the moment when the pores gradually collapse. Therefore, there are different degrees of residual materials in the pores of specimens.

2.5. Finite element analysis

The quasi-static uniaxial compression process was simulated by the finite element software ABAQUS, in which, the physical parameters of the TPU material are defined in Table 2, and the Mooney-Rivlin hyper-elastic constitutive model is adopted, where, the "dog bone" uniaxial tensile test was used to obtain hyper-elastic isometric test data.

The specimens were made of solid elements with a hexahedral mesh with a mesh size of 0.5 mm, and the upper and lower steel plates are set as discrete rigid bodies, more than 240,000 elements. To facilitate adding boundary conditions, set the reference point to couple the rigid body. The explicit dynamic solution methods were used for analysis, and the contact between the steel plate and the specimen was set as general contact, the tangential behavior was set as frictional contact, the normal behavior was set as "hard" contact, and the friction coefficient was set as 0.2. The reference point of the lower steel plate is set as a fixed constraint, and the axial displacement of the reference point of the upper steel plate is 35mm. Then submit homework, the deformation modes and load-bearing curves of the specimens are analyzed in the post-processing module.

The finite element analysis was performed on the specimens L-1, L-2, L-4 and L-5 respectively. The comparison between the compressive stress-strain curve and the deformation mode is shown in Figure 5. It can be seen that the finite element results are basically consistent with the experimental results of the compression curve trend, but there are errors in each specimen in different compression stages. The finite element results of the specimen L-1 in the elastic stage are significantly higher than the experimental results, which is due to the manufacturing defect in the 3D printing process. When preparing the specimen, the printing nozzle runs according to the program of printing the outer wall first and then filling the inner wall, which leads to obvious incomplete filling during the filling process, forming tiny filling gaps. In addition, the overlap ratio between the filaments and the adhesive force during filling also are the source of the formation of tiny gaps, which in turn can significantly affect the strength of the specimen. Meanwhile, the finite element results of the strength of several specimens in the compacted region are lower than the experimental results. This is because residual filaments will appear when the print nozzle travels empty in the specimen gap, which causes the specimen to be squeezed and compacted in advance, thereby increasing the strength. The above analysis on the source of errors can be well confirmed by comparing the deformation modes. The finite element results verify the reliability of the lattice structure model and the accuracy of the experimental results. The analysis in the second section is carried out experimentally.
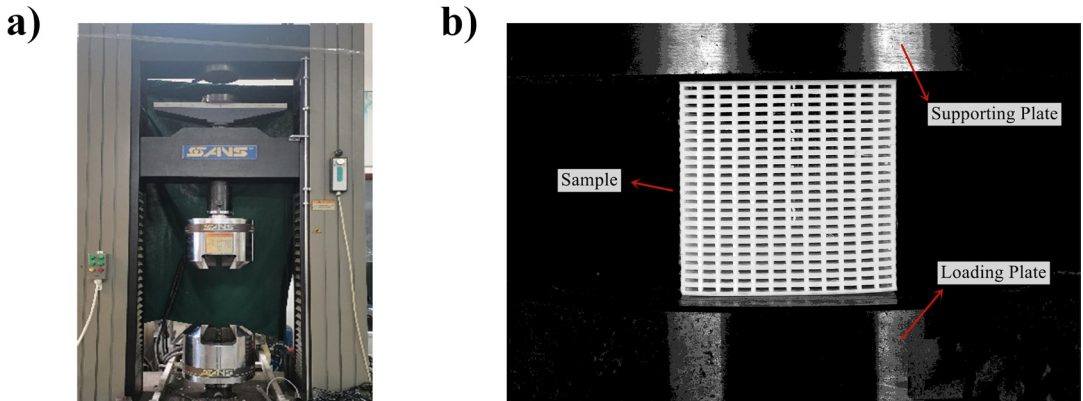

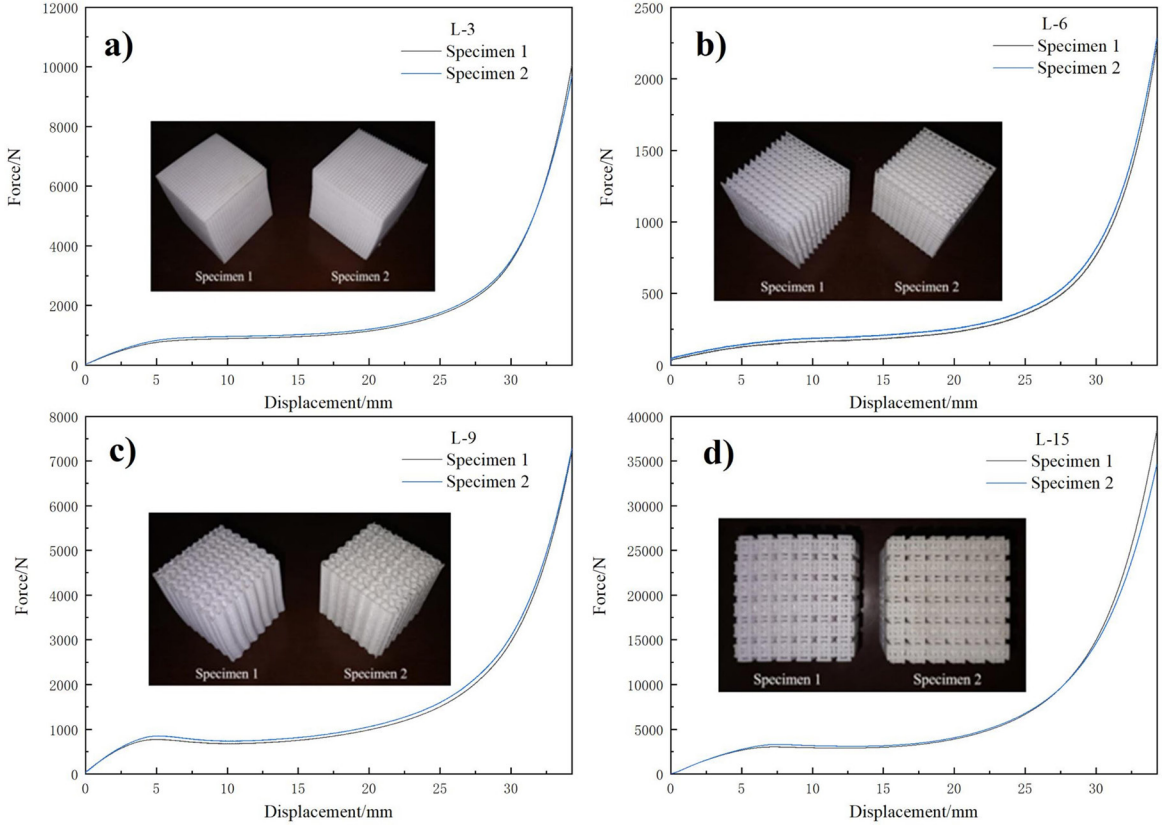**Figure 3.** a) Universal testing machine CMT5305, b) Experimental loading device.

Figure 4. Experimental force-displacement curves of several representative structures: a) L-3, b) L-6, c) L-9, d) L-15.

3. Results and Discussions

The mechanical properties are summarized based on the experimental results and finite element results of the lattice structure. From the compression stress-strain curve of the specimen, it can be seen that the quasi-static compression process can be divided into three stages. The linear elastic stage caused by the bending deformation of the line when the strain is small. The platform stage where the stress is almost constant in which the pores start collapse due to elastic buckling deformation of the line. And the compacting stage at large strains, the pores completely collapse at this stage, which causing the lines to contact each other and accumulate, and the stress to rise sharply. From the deformation mode of the specimen, the lattice structures show buckling deformation, which is mainly due to the pore distribution inside the structure and the line arrangement form. In addition, the friction factor between the fixture and the specimen is also one of the reasons. The analysis is carried out in section 2.4.

3.1. Index of mechanical properties

Since there are differences in the quality of different types of structures with same dimensions 49mm×49mm×49mm, the *SEA* indicators are used to evaluate the energy absorption capabilities of the lattice structure, in which *SEA* represents the SEA, and its expression is presented as in Equation 2,

$$SEA = \frac{EA}{M} \tag{2}$$

where, M is the total mass, and EA is the part of the area under the load displacement curve under a certain compressive strain, and its expression is presented as in Equation 3,

$$EA = \int_0^\varepsilon \sigma(\varepsilon)d\varepsilon \tag{3}$$

where, ε is the compressive strain, and $\sigma(\varepsilon)$ is the stress under the instantaneous compressive strain. In addition, the platform stress σ_p of each specimen is calculated, and the platform stress calculation formula is presented as in Equation 4,

$$\sigma_p = \frac{\int_{\varepsilon_a}^{\varepsilon_b} \sigma(\varepsilon)d\varepsilon}{\varepsilon_b - \varepsilon_a} \tag{4}$$

where, ε_a and ε_b are the strain at the initial time and the strain at the end of the platform stage, refer to literature[40], which selects the strain range of the platform as 0.2~0.4.

3.2. Geometric parameter analysis

3.2.1. Effect of strut distance

The schematic plan view of the specimen with different strut distance as shown in Figure 6. Figure 7 shows the stress-strain curves and the platform stress and SEA of three different strut distance lattice structures. It can be
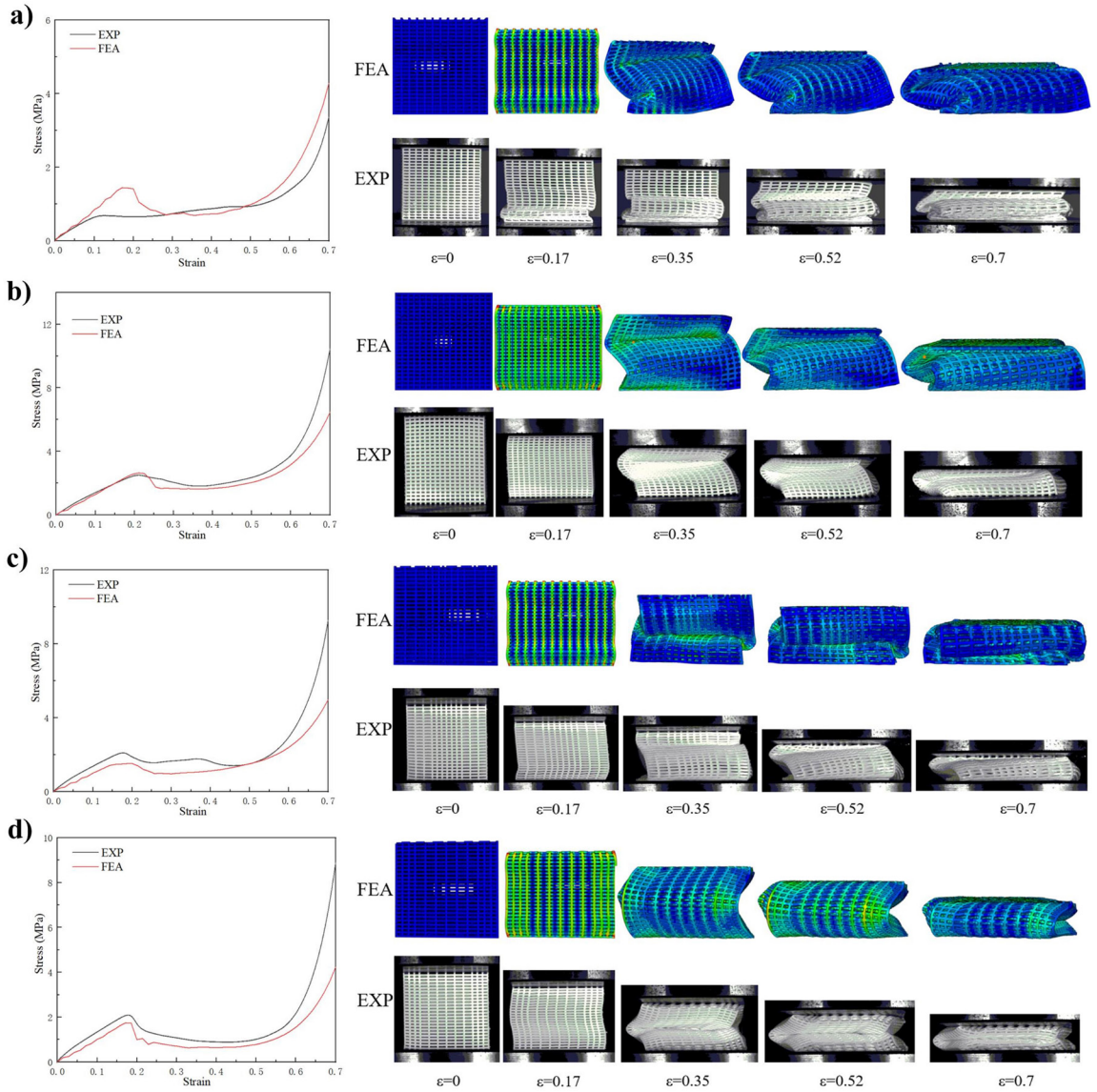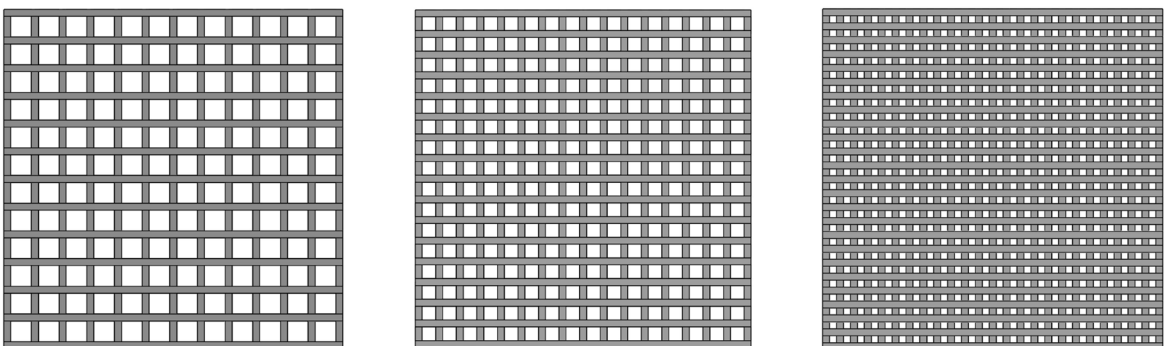
Figure 5. Comparison of experiment and simulation stress-strain curves and deformation mode: a) L-1, b) L-2, c) L-4, d) L-5.

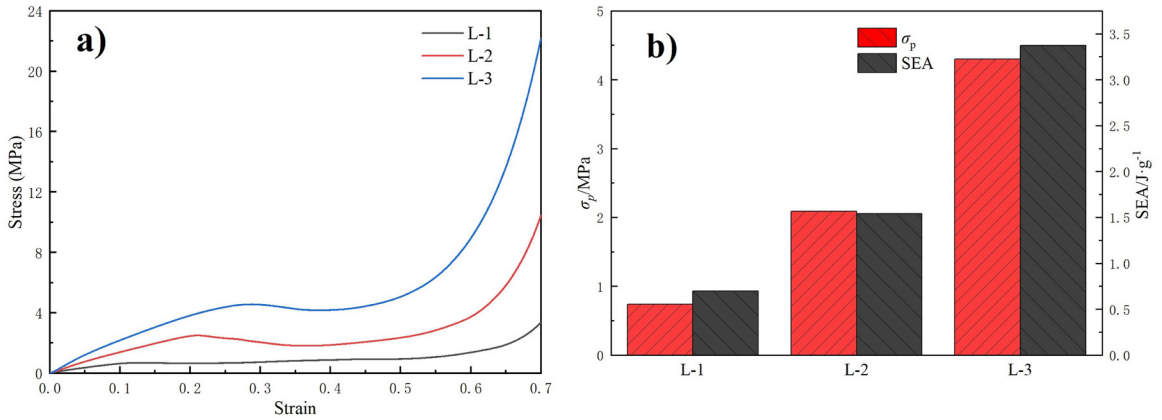**Figure 6.** Plane diagrams of specimens with different strut distances.

Figure 7. a) Stress-strain curves of different strut distance, b) Platform stress and SEA of different strut distance.
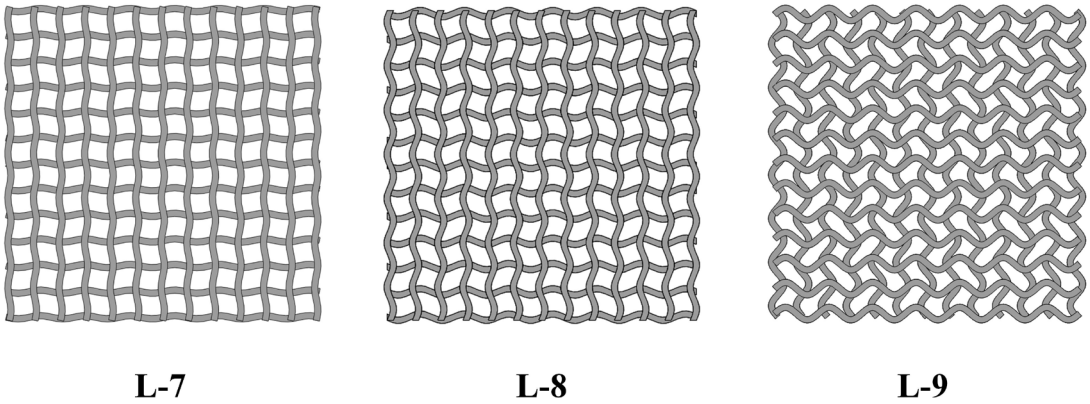

Figure 8. Plane diagrams of specimens with different curvatures.

seen that the smaller the strut distance, the less the pores to collapse, and the earlier the layers contact and accumulate. The platform stress and SEA also increase with the decrease of the strut distance, where, the platform stress of specimen L-3 is 481% higher than specimen L-1, and the SEA is 382% higher than specimen L-1.

3.2.2. Effect of curvature

Figure 8 shows the plan view of the specimen with different curvatures. Figure 9 shows the stress-strain curves and mechanical property indicators of three different line curvature lattice structures, it can be seen that specimen L-7 is the first to undergo elastic buckling deformation, and the pore collapse process is the longest. Although the pores of specimen L-8 began to collapse at the latest, it didn't take as fast as specimen L-9 to reach the compaction strain. It can be seen from Figure 8b that the platform stress and SEA are both increase with the increase of curvature, the platform stress of specimen L-9 is 146% higher than specimen L-7, and the SEA is 157% higher than specimen L-7.

3.2.3. Effect of strut style and arrangement form

Figure 10 shows the plan view of the specimen with different strut styles and arrangement forms. Figure 11 shows the stress-strain curves and mechanical properties of the lattice structure with different strut styles and arrangements, it can

be seen that the specimen L-12 has higher strength, which is because the specimen didn't undergo buckling deformation. Comparing with the experimental results of the same type, it can be seen that no matter what the strut styles are, when (0°/90°) orthogonal arrangement, the compressive stress-strain curve is almost the same, the difference between platform stress and SEA is very small either, but when (45°/135°) orthogonal arrangement, the lattice structure has higher strength and stronger energy absorption capacity, where, the platform stress of specimen L-6 is 12% higher than specimen L-1, and the SEA is 53% higher than specimen L-1, the platform stress of specimen L-12 is 199% higher than specimen L-7, and the SEA is 190% higher than specimen L-7. In addition, under the same arrangement, sine curve has higher strength and stronger energy absorption capacity than straight lines, where, the platform stress of specimen L-7 is 8% higher than specimen L-1, and the SEA is only 3% higher than specimen L-1, the platform stress of specimen L-12 is 188% higher than specimen L-6, and the SEA is 94% higher than specimen L-6.

3.2.4. Effect of the gradient form strut distance

Figure 12 shows the plan view of the specimen with different gradient form strut distances. The stress-strain curves and mechanical performance indicators under different forms of strut distance are shown in Figure 13, it can be seen that no
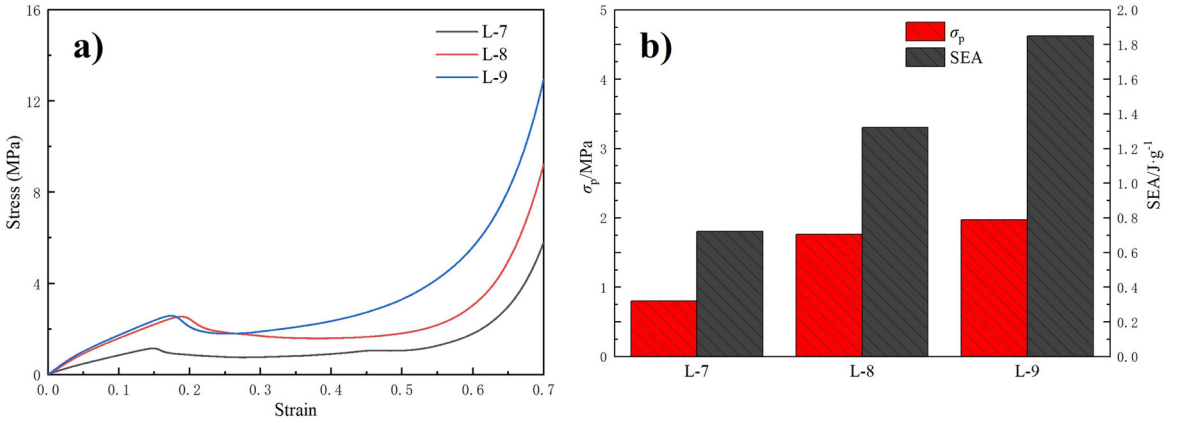
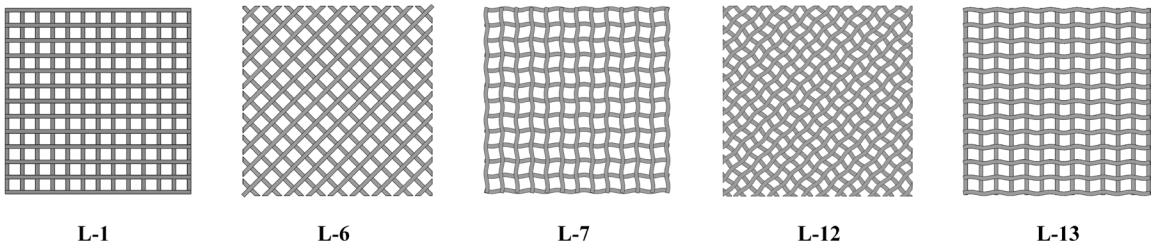**Figure 9.** a) Stress-strain curves of different curvature k, b) Platform stress and SEA of different curvature k.

Figure 10. Plane diagrams of specimens with different strut styles and arrangement forms.
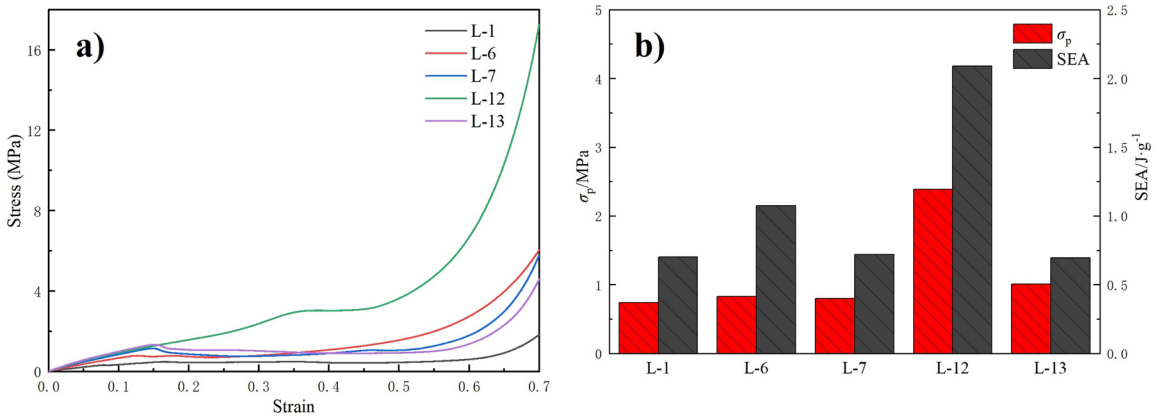

Figure 11. a) Stress-strain curves of different styles and arrangements, b) Platform stress and SEA of different styles and arrangements.

matter what the strut styles are, the strength and the energy absorption capacities of gradient form specimens are better than uniform strut distance, and the inward gradient form has the highest strength. The platform stress of specimen L-4 is 126% higher than specimen L-1, and the SEA is 75% higher than specimen L-1, the platform stress of specimen L-10 is 186% higher than specimen L-7, and the SEA is 107% higher than specimen L-7.

3.2.5. Effect of lattice height

Taken specimens L-1 and L-4 as an example, using lattice height as a variable, and taken the layer heights with 16 layers,

32 layers, and 49 layers to perform a quasi-static experiment with the same scheme. Figure 14 shows the plan view of the specimen with different lattice heights. The results as shown in Figure 15, it can be seen that the smaller the lattice height, the higher the strength and the SEA. Because the specimen with a small height is not easy to lose stability, the strength of the specimen can be maintained. The platform stress of specimen L-1-16 layer is 305% higher than specimen L-1-49 layer, and the SEA is 173% higher than specimen L-1-49 layer, the platform stress of specimen L-4-16 layer is 53% higher than specimen L-4-49 layer, and the SEA is 52% higher than specimen L-4-49 layer.
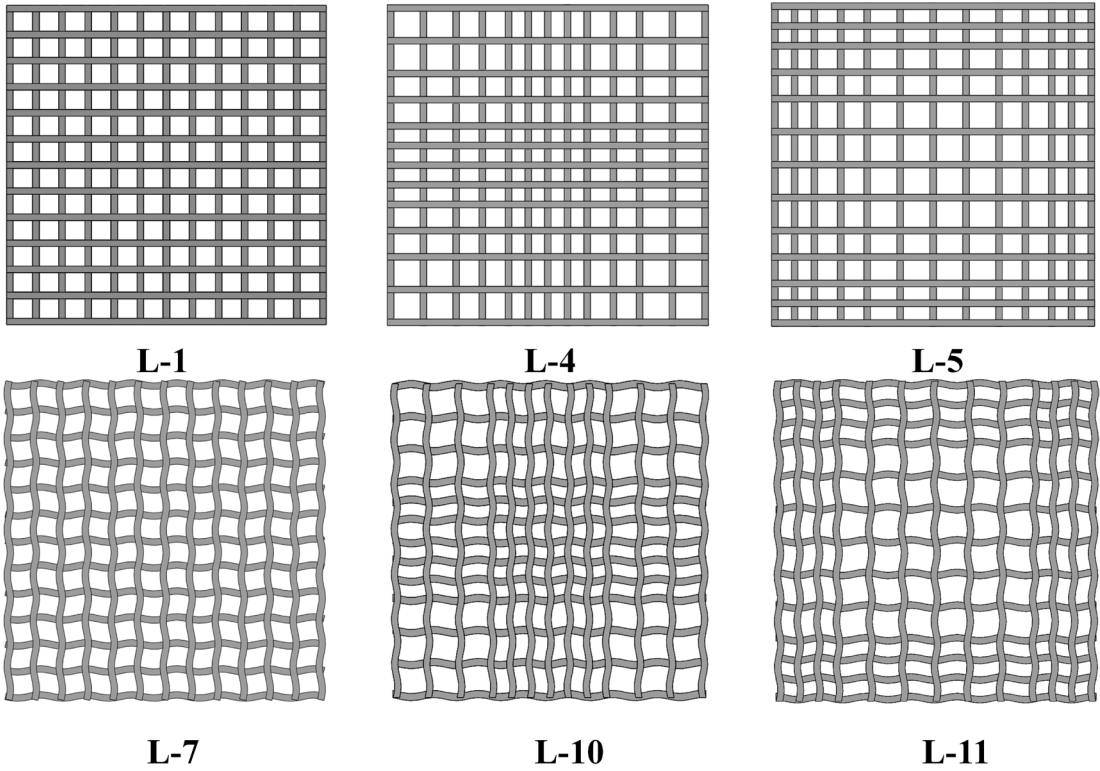
Figure 12. Plane diagrams of specimens with different gradient form strut distances.
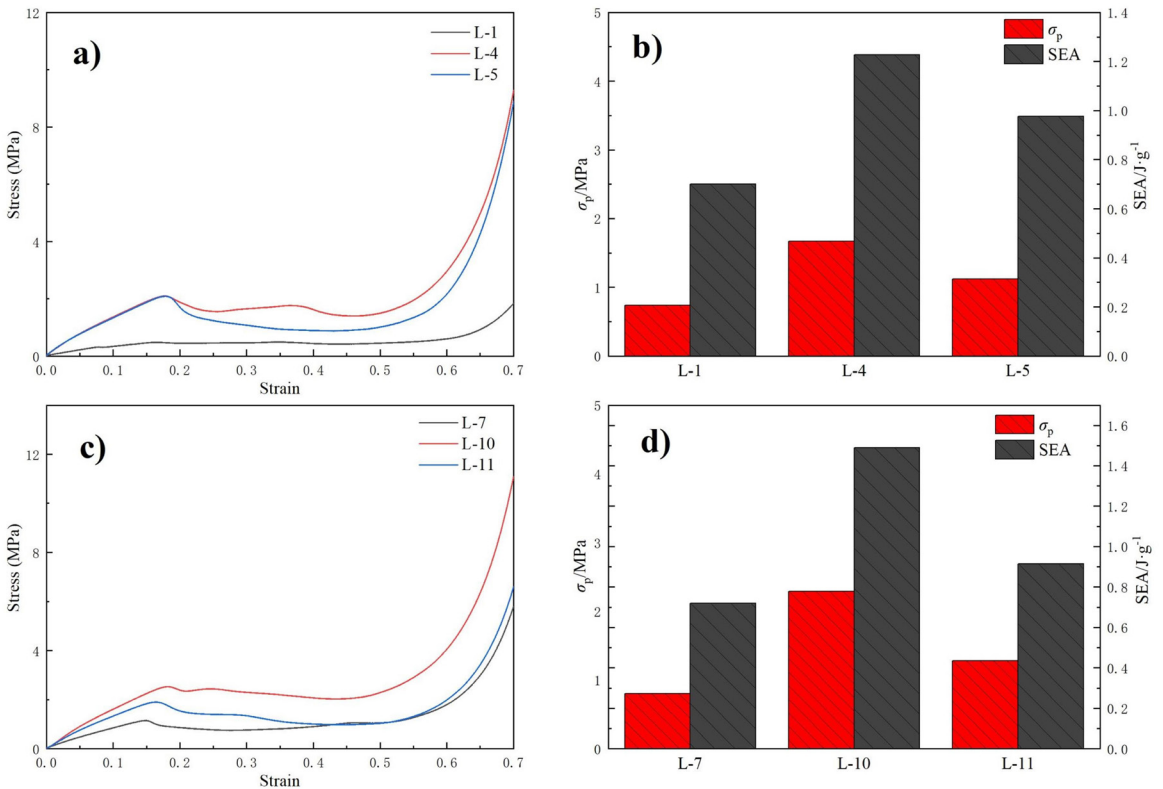

Figure 13. a) Stress-strain curves of different strut distance gradients when straight line, b) Platform stress and SEA of different strut distance gradients when straight line, c) Stress-strain curves of different strut distance gradients when curve line, d) Platform stress and SEA of different strut distance gradients when curve line.
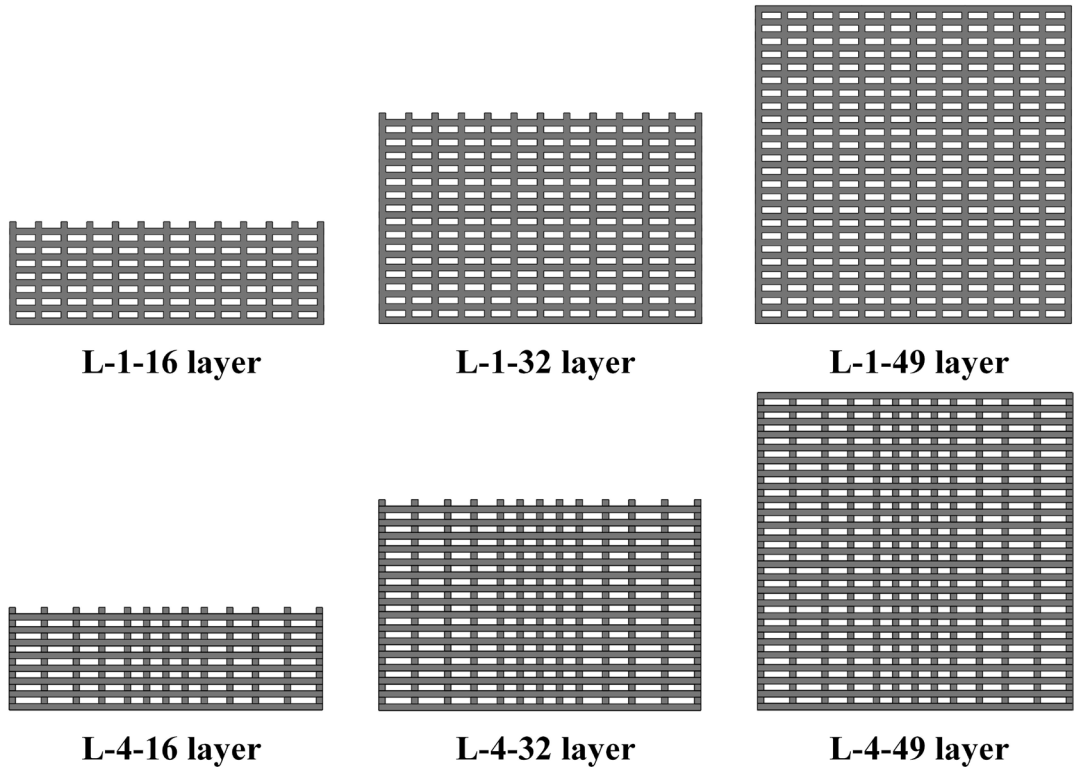
Figure 14. Plane diagrams of specimens with different lattice heights.
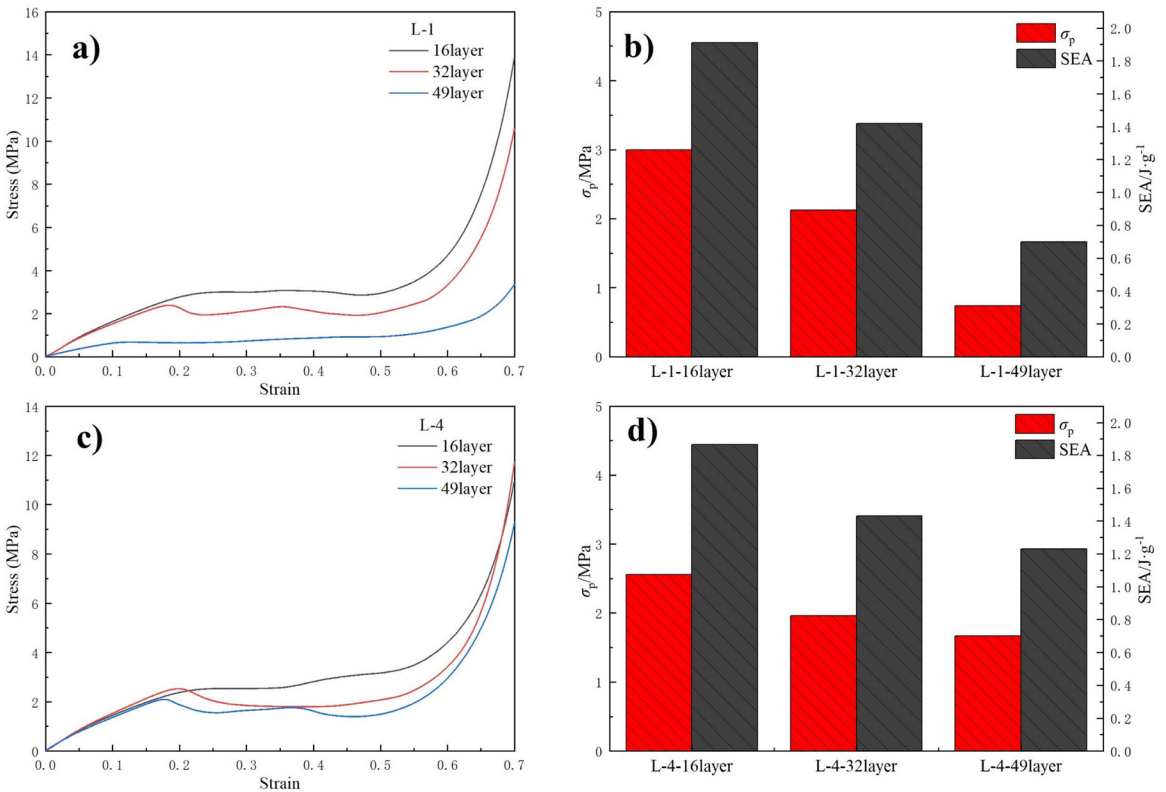

Figure 15. a) Stress-strain curves of different lattice height (L-1), b) Platform stress and SEA of different lattice height(L-1), c) Stress-strain curves of different lattice height (L-4), d) Platform stress and SEA of different lattice height (L-4).

3.2.6. Effect of honeycomb lattice structure

Figure 16 shows the plan view of the specimen with different honeycomb lattice structures. Figure 17a shows the stress-strain curves of several porous honeycomb lattice structures, it can be seen that the strength of the three honeycomb lattices is significantly improved compared with the traditional face-centered cubic lattice structure. Under 70% strain, the peak stress of the three honeycomb lattices can reach 30MPa. Figure 17b shows the platform stress and the SEA of three porous honeycomb lattices, where, the platform stress of specimen L-15 is 86% and 3% higher than that of L-14 and L-16, the SEA is 55% and 8% higher than that of L-14 and L-16, respectively.

3.3. Relation between platform stress and SEA

Figure 18 shows *SEA* as a function of σ_p, considering strut distance, curvature, strut style and arrangement, gradient strut distance, and lattice height and other parameters. The greater the energy absorption *SEA* and the platform stress σ_p, the better the energy absorption of the lattice structure, so the data point on the upper right of the figure corresponds to the best energy absorption performance. It can be seen that the porous honeycomb cubic lattice (especially the positive and negative Poisson's ratio topology configuration) has better

energy absorption capacity than other lattice structures. Meanwhile, it is worth noting that the L-3 lattice has a higher energy absorption capacity due to its small strut distance and dense pores, so it has a large *SEA* and σ_p value. Except for the honeycomb lattice and the L-3 lattice, the difference between the *SEA* and σ_p values of the lattice under other modified parameters is very small. In addition, Figure 18 has a linear fit to all data points, the results confirm that the energy absorption *SEA* and the platform stress σ_p have a good correlation, indicating that both *SEA* and σ_p can be used to evaluate the energy absorption capacity of the lattice structure.

3.4. Deformation mode

Figure 19 shows the deformation modes of each specimen at the same time when the compressive strain ε=0.35 and ε=0.7, it can be seen that, except specimens L-12 and L-16, other lattice structures show different instability deformation in different positions. The local deformation diagram indicated that the instability deformation process is from the instability position to collapse layer by layer to compaction. Different structures have different instability positions and instability degrees, in which specimen L-1 and L-7 first collapsed from the top or bottom, while other specimens began to collapse in the middle or near the middle. Analyzing the internal geometric
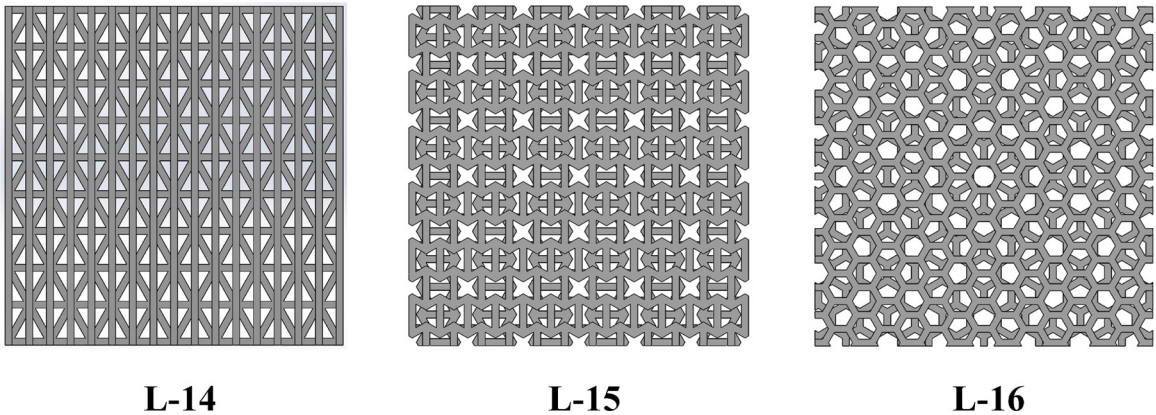

L-14   **L-15**   **L-16**

Figure 16. Plane diagrams of specimens with different honeycomb lattice structures.
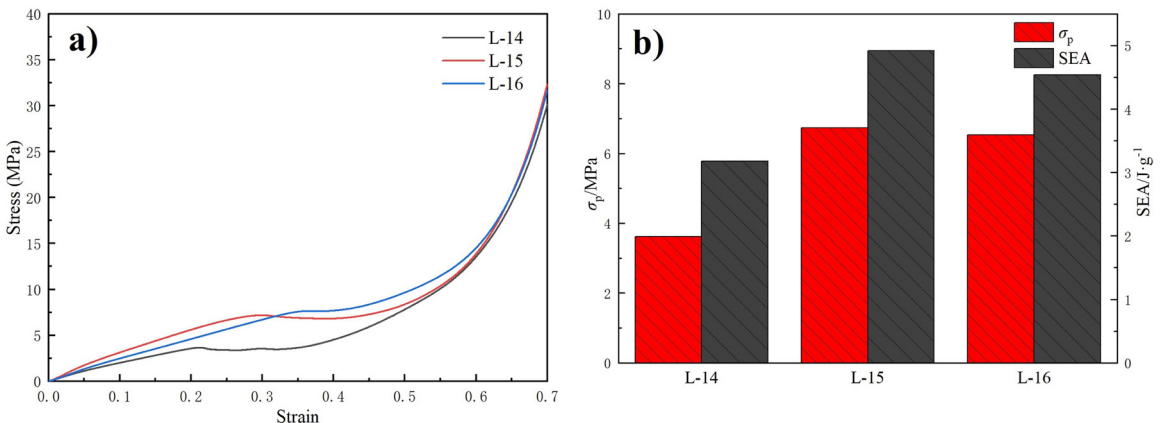

Figure 17. a) Stress-strain curves of different honeycomb lattice configurations, b) Platform stress and SEA of different honeycomb lattice configurations.
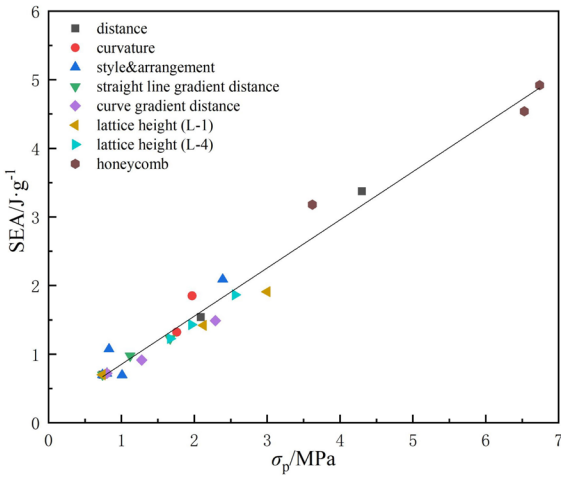
Figure 18. Relation between platform stress and SEA.

variables of the structure, it shows that the smaller the strut distance, the greater the curvature of the curve, and the closer the instability position is to the middle. The strut distance of the inward gradient form is less unstable than the outward gradient form, and the porous honeycomb lattice structure has the smallest instability deformation compared with other lattices with geometric parameter variables. In addition, there are some special phenomenon of instability, in which specimen L-5 shrinks inwardly with lateral instability, and the upper and lower contact surfaces are turned outward. Specimen L-12 has no instability due to its internal strut style and arrangement, so the curve spline has the ability to resist buckling deformation under the (45°/135°) orthogonal arrangement. Symmetrical instability occurred on the upper and lower sides of specimen L-14, and the instability mode was in an "S" shape, specimen L-16 exhibited a negative poisson's ratio effect that contracted inward from both sides during the compression process.
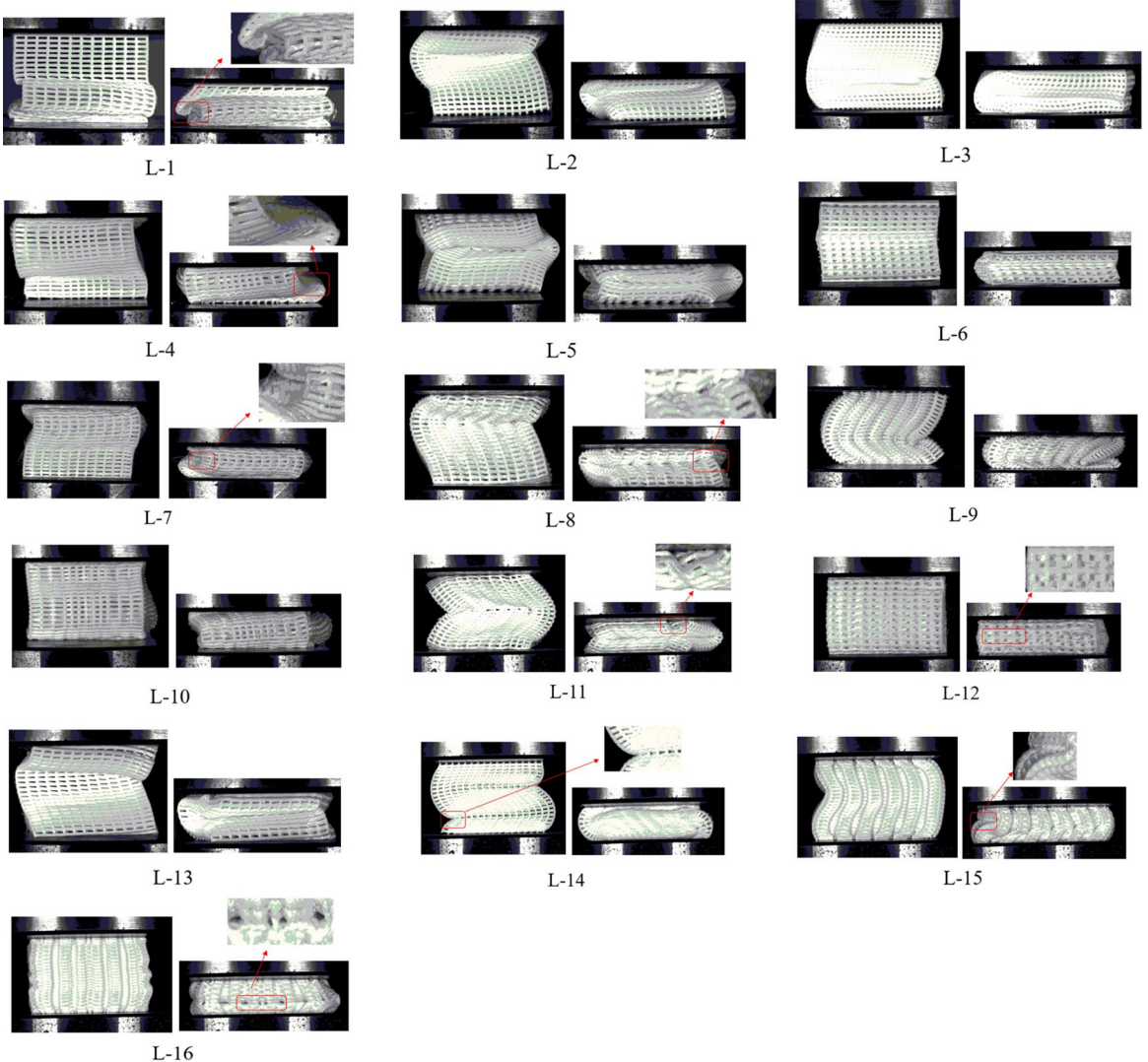

Figure 19. Deformation mode of lattice structures.

4. Conclusions

In this paper, several types of cubic lattice structures are designed based on the face-centered cubic structure, which undergoing quasi-static uniaxial compression experiments. By analyzing the results, the following conclusions can be obtained.

(1) When the relative density is the same, the selection of sinusoidal struts with larger curvature, the arrangement of 45°/135°, and the inward gradient of the strut distance can all improve the energy absorption characteristics of the structure. Compared with the traditional face-centered cubic structure (specimen L-1), the SEA of the structure with the strut curvature of 0.25, the 45°/135° arrangement of the sinusoidal struts, and the inward gradient of the strut distance is improved by 64% , 190%, and 107%;

(2) The smaller the lattice height, the less prone to buckling deformation of the structure.

(3) Compared with the traditional face-centered cubic structure, the strength and the energy absorption capacities of the porous honeycomb lattice structure are significantly improved. The SEA of triangular, re-entrant and hexagonal honeycomb structures is 354%, 603% and 548% higher than that of basic structures respectively.

(4) Lattice structures will undergo lateral buckling deformation due to its internal line arrangement and pore density during compression. Reducing strut distance, increasing the curvature can all improving the ability of the structure to resist buckling deformation, by contrast, the porous honeycomb lattice structure has the strongest resistance to buckling deformation.

5. Acknowledgments

6. References

1. Nian Y, Wan S, Zhou P, Wang X, Santiago R, Li M. Energy absorption characteristics of functionally graded polymer-based lattice structures filled aluminum tubes under transverse impact loading. Mater Des. 2021;209:110011.

2. Liu L, Wen X-Y, Wang D-S. A new lattice hierarchy: hamiltonian structures, symplectic map and N-fold Darboux transformation. Appl Math Model. 2019;67:201-18.

3. Lei H-Y, Li J-R, Xu Z-J, Wang Q-H. Parametric design of Voronoi-based lattice porous structures. Mater Des. 2020;191:108607.

4. Zhang H-R, Zhou H, Zhou Z-X, Zeng H, Zhang X, Yang J, et al. Energy absorption diagram characteristic of metallic self-supporting 3D lattices fabricated by additive manufacturing and design method of energy absorption structure. Int J Solids Struct. 2021;226:111082.

5. Alkebsi EAA, Ameddah H, Outtas T, Almutawakel A. Design of graded lattice structures in turbine blades using topology optimization. Int J Comput Integrated Manuf. 2021;34(4):370-84.

6. Zhong T-L, He K-T, Li H-X, Yang L. Mechanical properties of lightweight 316L stainless steel lattice structures fabricated by selective laser melting. Mater Des. 2019;181:108076.

7. Habib FN, Iovenitti P, Masood SH, Nikzad M. Fabrication of polymeric lattice structures for optimum energy absorption using Multi Jet Fusion technology. Mater Des. 2018;155:86-98.

8. Xu B, Yin S, Wang Y, Li H, Zhang B, Ritchie RO. Long-fiber reinforced thermoplastic composite lattice structures: fabrication and compressive properties. Compos, Part A Appl Sci Manuf. 2017;97:41-50.

9. Zhang X, Xue Z, Cheng Q, Ji Y. Optimization design of variable density lattice structure for additive manufacturing. Energy. 2022;242:122554.

10. Fernandes RR, Tamijani AY. Design optimization of lattice structures with stress constraints. Mater Des. 2021;210:110026.

11. Niknam H, Akbarzadeh AH. Graded lattice structures: simultaneous enhancement in stiffness and energy absorption. Mater Des. 2020;196:109129.

12. Nasim M, Galvanetto U. Mechanical characterisation of additively manufactured PA12 lattice structures under quasi-static compression. Mater Today Commun. 2021;29:102902.

13. Mahbod M, Asgari M, Mittelstedt C. Architected functionally graded porous lattice structures for optimized elastic-plastic behavior. Proc Inst Mech Eng Pt L-J Mater Des Appl. 2020;234(8):1099-116.

14. Teimouri M, Asgari M. Mechanical performance of additively manufactured uniform and graded porous structures based on topology-optimized unit cells. Proc Inst Mech Eng, C J Mech Eng Sci. 2021;235(9):1593-618.

15. Teimouri M, Mahbod M, Asgari M. Topology-optimized hybrid solid-lattice structures for efficient mechanical performance. Structures. 2021;29:549-60.

16. Alomar Z, Concli F. Compressive behavior assessment of a newly developed circular cell-based lattice structure. Mater Des. 2021;205:109716.

17. Ding R, Du B, Yao J, Zheng H, Guo Y, Kang Z. Mechanical properties and deformation behaviour of ARCH and BCT lattice structures manufactured by selective laser melting. IOP Conf Ser Mater Sci Eng. 2020;727(1):012001.

18. Yang C-X, Li Q-M. Advanced lattice material with high energy absorption based on topology optimisation. Mech Mater. 2020;148:103536.

19. Wei Y-L, Yang Q-S, Liu X, Tao R. Multi-bionic mechanical metamaterials: A composite of FCC lattice and bone structures. Int J Mech Sci. 2022;213:106857.

20. Javaid M, Haleem A, Singh RP, Suman R, Rab S. Role of additive manufacturing applications towards environmental sustainability. Adv Ind Eng Polym Res. 2021;4(4):312-22.

21. Chen L-Y, Liang S-X, Liu Y, Zhang L-C. Additive manufacturing of metallic lattice structures: unconstrained design, accurate fabrication, fascinated performances, and challenges. Mater Sci Eng Rep. 2021;146:100648.

22. Liu Y, Zhang J, Gu X, Zhou Y, Yin Y, Tan Q, et al. Mechanical performance of a node reinforced body-centred cubic lattice structure manufactured via selective laser melting. Scr Mater. 2020;189:95-100.

23. Verma S, Yang C-K, Lin C-H, Jeng JY. Additive manufacturing of lattice structures for high strength mechanical interlocking of metal and resin during injection molding. Additive Manufacturing. 2022;49:102463.

24. Wang P, Yang F, Ru D, Zheng B, Fan H. Additive-manufactured hierarchical multi-circular lattice structures for energy absorption application. Mater Des. 2021;210:110116.

25. Li T, Jarrar F, Abu Al-Rub R, Cantwell W. Additive manufactured semi-plate lattice materials with high stiffness, strength and toughness. Int J Solids Struct. 2021;230-231:111153.

26. Kostadinov A, Yan L, Teo AQA, O'Neill G. Slanted and cluttered: solving deficiencies in SLM-manufactured lattice geometries. Mater Des. 2021;211:110130.

27. Silva RG, Torres MJ, Vinuela JZ, Zamora AG. Manufacturing and characterization of 3D miniature polymer lattice structures using

fused filament fabrication. Polymers (Basel). 2021;13(4):635-635.

28. Chen W-J, Zeng X-R, Lai X-J, Li H, Fang WZ, Hou F. Suppression effect and mechanism of platinum and nitrogen-containing silane on the tracking and erosion of silicone rubber for high-voltage insulation. ACS Appl Mater Interfaces. 2016;8(32):21039-45.

29. Berahman R, Raiati M, Mazidi MM, et al. Preparation and characterization of vulcanized silicone rubber/halloysite nanotube nanocomposites: effect of matrix hardness and HNT content. Mater Des. 2016;104:333-45.

30. Zhao J, Luo G-X, Wu J, Xia H. Preparation of microporous silicone rubber membrane with tunable pore size via solvent evaporation-induced phase separation. ACS Appl Mater Interfaces. 2013;5(6):2040-6.

31. Liu H, Ng B-F. Dynamic response of density-graded foam subjected to soft impact. Compos Struct. 2022;284:115145.

32. Silva RM, Rodrigues JL, Pinto VV, Ferreira MJ, Russo R, Pereira CM. Evaluation of shock absorption properties of rubber materials regarding footwear applications. Polym Test. 2009;28(6):642-7.

33. De León AS, Domínguez-Calvo A, Molana SI. Materials with enhanced adhesive properties based on acrylonitrile-butadiene-styrene (ABS)/thermoplastic polyurethane (TPU) blends for fused filament fabrication (FFF). Mater Des. 2019;182:108044.

34. Wang P, Yang F, Li P-H, Zheng B, Fan H. Design and additive manufacturing of a modified face-centered cubic lattice with enhanced energy absorption capability. Extreme Mech Lett. 2021;47:101358.

35. Sun F, Lai C, Fan H. In-plane compression behavior and energy absorption of hierarchical triangular lattice structures. Mater Des. 2016;100:280-90. http://dx.doi.org/10.1016/j.matdes.2016.03.023.

36. Wang S, Deng C, Ojo O, Akinrinlola B, Kozub J, Wu N. Design and modeling of a novel three dimensional auxetic reentrant honeycomb structure for energy absorption. Compos Struct. 2022;280:114882.

37. Jam A, Du Plessis A, Lora C, Raghavendra S, Pellizzari M, Benedetti M. Manufacturability of lattice structures fabricated by laser powder bed fusion: a novel biomedical application of the beta Ti-21S alloy. Additive Manufacturing. 2022;50:102556.

38. Segovia-Chaves F, Vinck-Posada H, Navarro-Barón E. Photonic band structure in a two-dimensional hexagonal lattice of equilateral triangles. Phys Lett A. 2019;383(25):3207-13.

39. Lin K, Gu D, Hu K, Yang J, Wang H, Yuan L, et al. Laser powder bed fusion of bio-inspired honeycomb structures: effect of twist angle on compressive behaviors. Thin-walled Struct. 2021;159:107252.

40. Silva RG, Estay CS, Pavez GM, Viñuela JZ, Torrer MJ. Influence of geometric and manufacturing parameters on the compressive behavior of 3D printed polymer lattice structures. Materials (Basel). 2021;14(6):1462-1462.